Atomic Layer Deposition of Ruthenium Dioxide Based on Redox Reactions between Alcohols and Ruthenium Tetroxide

Reference:

Nithin Poonkottil, Matthias M Minjauw, Andreas Werbrouck, Stefano Checchia, Eduardo Solano, Mikko Nisula, Alexis Franquet, Christophe Detavernier, Jolien Dendooven; Chem. Mater. 2022, 34, 19, 8946–8958

Full text (Publisher's DOI): doi.org/10.1021/acs.chemmater.2c02292

Atomic Layer Deposition of Ruthenium Dioxide based on Redox Reactions between Alcohols and Ruthenium Tetroxide

Nithin Poonkottil, [†, ▽] Matthias M. Minjauw,[†, ▽] Andreas Werbrouck,[†] Stefano Checchia,[#] Eduardo Solano,[$] Mikko Nisula,[†] Alexis Franquet,[‡] Christophe Detavernier[†] and Jolien Dendooven[†,*]

† Department of Solid State Sciences, COCOON, Ghent University, Krijgslaan 281/S1, B-9000 Ghent, Belgium

‡ IMEC, Kapeldreef 75, B-3001 Heverlee (Leuven), Belgium

$ NCD-SWEET beamline, ALBA Synchrotron Light Source, Cerdanyola del Valles 08290, Spain

ESRF Synchrotron, ID15A beamline, Avenue des Martyrs, CS40220, 38043, Grenoble, France

Abstract

Atomic layer deposition (ALD) of ruthenium dioxide (RuO_2) thin films using metalorganic precursors and O_2 can be challenging because the O_2 dose needs to be precisely tuned and significant nucleation delays are often observed. Here, we present a low-temperature ALD process for RuO_2 combining the inorganic precursor ruthenium tetroxide (RuO_4) with alcohols. The process exhibits immediate linear growth at 1 Å/cycle when methanol is used as reactant at deposition temperatures in the range of 60 to 120°C. When other alcohols are used, the growth per cycle increases with an increasing number of carbon atoms in the alcohol chain. Based on X-ray photoelectron spectroscopy (XPS) and conventional X-ray diffraction, the deposited material is thought to be amorphous RuO_2. Interestingly, pair distribution function (PDF) analysis shows that structural order exists up to 2-3 nm. Modelling of the PDF suggests the presence of Ru nanocrystallites within a predominantly amorphous RuO_2 matrix. Thermal annealing to 420°C in inert atmosphere crystallizes the films into rutile RuO_2. The films are conductive, as is evident from a resistivity value of 230 μΩ·cm for a 20 nm film grown with methanol, and the resistivity decreased to 120 μΩ·cm after crystallization. Finally, based on in situ mass spectrometry, in situ infrared spectroscopy and in vacuo XPS studies, an ALD reaction mechanism is proposed, involving partial reduction of the RuO_2 surface by the alcohol, followed by re-oxidation of the surface by RuO_4 and concomitant deposition of RuO_2.

Introduction

Ruthenium dioxide (RuO_2) is known for its very low resistivity value (~ 35 μΩ.cm), high chemical stability, and a work function even higher than metallic Ru (5.1 eV for RuO_2 and 4.1 eV for Ru).[1-3] RuO_2, in both amorphous and crystalline forms, is interesting for various applications, especially in electrochemical devices.[4-8] Crystalline RuO_2 is a promising material for gas-evolving reactions,[9-11] such as hydrogen, oxygen and chlorine evolutions, whereas amorphous ruthenium dioxide is suitable for electrochemical pseudocapacitor applications.[5, 8, 12-13] Over the past 40 years, it has been used as a dimensionally stable anode (DSA) for the chlorine-alkali electrocatalysis.[14-16] RuO_2 based catalysts have emerged as promising heterogenous catalysts for low-temperature dehydrogenation of molecules like NH_3,[17] HCl,[18] and methanol.[19] Among the different transition metal oxides (TMOs), RuO_2 has attracted immense attention for supercapacitor applications, owing to its high conductivity, excellent cyclic performance, and high specific capacitance.[2, 20-23] To avoid the leakage current, a very high work function value for the metal electrode is necessary. This fact gives a clear advantage for RuO_2 as electrodes for the capacitors in DRAM over the currently integrated TiN (~4.2 eV) and even metallic Ru.[1] In addition, it has been used as a positive electrode material for lithium ion batteries,[24-25] and thin RuO_2 films act as excellent barriers against O_2 diffusion.[26]

RuO_2 thin films have been grown for various purposes using techniques such as direct deposition by magnetron sputtering[27-28] or reactive sputtering of Ru.[29] The other commonly employed techniques are pulsed laser deposition (PLD)[30-31], electrodeposition from aqueous solution[32] or cyclic voltammetry,[33] sol-gel spin coating method,[34] metal organic chemical vapor deposition (MOCVD),[35-36] chemical vapor deposition (CVD),[37-38] pulsed-CVD,[39] and atomic layer deposition (ALD).[40-50] Among those techniques to prepare RuO_2 thin films, ALD offers uniform and conformal growth over 3-dimensional substrates without compromising the precise control over thickness and composition.[51-53]

Previous reports on ALD of RuO_2 employed organometallic precursors such as bis(cyclopentadienyl) Ru(II) [$RuCp_2$],[48] bis(ethylcyclopentadienyl) Ru(II) [$Ru(EtCp)_2$],[43, 46-47, 50, 54-55] and bis(2,2,6,6-tetramethyl-3,5-heptanedinonato)(1,5-cyclooctadiene) Ru(III) [Ru(thd)2(cod)],[56] the most commonly used precursor being [$Ru(EtCp)_2$]. Recent reports make use of zero-valent ruthenium complexes like (1,5-

Hexadiene)(1-isopropyl-4-methylbenzene)ruthenium,[40] (η4-2,3-dimethylbutadiene)(tricarbonyl)ruthenium,[41] and (ethylbenzene)(1,3-butadiene)ruthenium.[44] In almost all cases, the co-reactant used is molecular O_2. The reaction mechanism proposed by Aaltonen *et al*. illustrates the main challenge for depositing RuO_2 by ALD using an organometallic precursor and O_2 gas.[57] The authors found that the precursor molecules are partially oxidized into H_2O and CO_2 by (sub-) surface oxygen atoms upon adsorption, and the remaining part of the ligands are oxidized during the subsequent O_2 pulse. All the oxygen that adsorbs on the surface is used for the oxidation reaction with the precursor, such that metallic ruthenium, and not ruthenium dioxide, is formed in the resulting films. Hence, several authors reported the necessity of high oxygen partial pressures to synthesize RuO_2 by ALD.[46, 50] In addition to this, the formation of RuO_2 relies on different parameters including the deposition temperature[58] and the amount of Ru precursor adsorbed on the surface.[46]

Given the importance of RuO_2, it is highly desirable to have ALD chemistries that offer solutions to the above-mentioned drawbacks. In this scenario, we report the synthesis of RuO_2 using ruthenium tetroxide (RuO_4) as the precursor and an alcohol as the co-reactant. In our previous works, we have demonstrated the suitability of RuO_4 as a Ru source for ALD of metallic Ru films, in combination with H_2[59] or H_2 plasma[60] as the co-reactant. The proposed reaction mechanism for the thermal process is given below.

(1) $Ru(s) + RuO_4(g) \rightarrow 2RuO_2(s)$

(2) $RuO_2(s) + 2H_2(g) \rightarrow Ru(s) + 2H_2O(g)$

The first reaction (1) shows the formation of a RuO_2 layer on a Ru surface when exposed to RuO_4. This reaction saturates because RuO_4 cannot dissociate on a RuO_2 surface. The deposited RuO_2 surface layer is then reduced to metallic Ru by H_2 in the next reaction (2).

In this work, we use the same Ru source, i.e., RuO_4, but in combination with alcohols to deposit RuO_2 films by ALD. Alcohols such as ethanol have been previously used as reducing agent to remove unwanted CuO_x layers formed on metallic Cu films upon ambient exposure.[61] Some of the ALD processes in the literature have also benefited from the use of alcohols as reducing agent.[62-64] So the starting hypothesis in this work was to use alcohols to partially reduce the RuO_2 surface formed upon the introduction of RuO_4. This would create a surface that is again oxidizable, enabling reaction with

RuO_4, and resulting in the deposition of stoichiometric RuO_2. Indeed, the use of methanol in combination with RuO_4 results in deposition of RuO_2 with a growth per cycle (GPC) of 1Å per cycle, a value which is shown to increase by choosing a higher alcohol homologue such as ethanol, 1-propanol, and 2-propanol. The use of RuO_4 as the Ru source, which has a high vapor pressure and is a liquid at room temperature, alleviates the need for organometallic precursors that are less reactive and require comparatively higher temperatures to convert into the gaseous phase. The issues with the careful tuning of the O_2 partial pressures are avoided by the oxidizing properties of RuO_4, combined with the alcohol as a gentle reducing agent. The processes introduced in this work (different alcohols in combination with RuO_4) do not show significant nucleation delays, whereas most processes reported so far, suffer from very long nucleation delays[41], up to several hundreds of cycles in some cases. Moreover, with deposition temperatures in the range of 60 to 120°C, the RuO_4/alcohol processes are compatible with temperature-sensitive substrates, offering another important advantage over the majority of processes that use metalorganic Ru precursors.

Experimental Section

ALD Synthesis

The RuO_2 thin films were grown in a custom-built ALD reactor described elsewhere.[65] The setup is equipped with a turbomolecular pump, which is connected to the vacuum chamber through a gate valve, such that a base pressure of 10^{-6} mbar is achieved. The sample is heated inside the chamber with a resistive heater. A solution of RuO_4 in a methyl-ethyl fluorinated solvent (ToRuS^{TM}), developed and produced by Air Liquide, was used as the Ru source.[66] The alcohols used as the reactants in this work, namely, methanol (99%), ethanol (98%), 1-propanol (99%), and 2-propanol (98%) were purchased from Sigma Aldrich. No carrier gas was used to supply the alcohols or RuO_4 to the chamber. The precursor containers were not heated, owing to the high vapor pressure of both precursors. The inlets of both precursors were kept at 65 °C. The chamber walls were kept at 90 °C to avoid condensation of the precursors. During both the precursor pulses and the co-reactant pulses, the gate valve to the turbomolecular pump was kept open, and the flow of the precursor gas was regulated by a needle valve, which caused the reactor pressure to increase to 4×10^{-3} mbar. H-terminated Si (Si-H) substrates were obtained by dipping Si with native oxide in a 2.5

% hydrogen fluoride solution for approximately 60 s and after that they were put in deionized water to wash away any remaining fluoride impurities. Then they were immediately transferred to the reactor for depositions. Metallic Ru films that will be described in this work are prepared by the RuO_4-H_2 ALD process, as reported before.[59]

Material and Process Characterization

X-ray reflectivity (XRR) and X-ray diffraction (XRD) measurements were performed using a Bruker D8 diffractometer[67-68] with Cu Kα radiation. The post-annealing of the deposited films in He and air was performed in a custom-built heating chamber mounted on a Bruker D8 diffractometer to enable *in situ* XRD characterization.[69] A linear detector was used to collect the diffracted X-rays at 2 s time intervals. SEM was performed using a FEI Quanta 200 F instrument combined with an EDAX silicon drift detector to perform energy dispersive X-ray spectroscopy (EDX). To verify the conformality of the RuO_2 ALD process, silicon micro-pillar substrates were used which were prepared using the Bosch Deep Reactive Ion Etching process.[70] Atomic Force Microscopy (AFM) was used in tapping mode to determine the roughness of the samples and was done using a Bruker Dimension Edge system.

Grazing incidence wide angle X-ray scattering (GIWAXS) measurements of the samples were performed at the NCD-SWEET beamline of the ALBA synchrotron, Spain. The X-ray energy used was 12.4 keV with a collimated beam size at the sample position of 50 x 150 um^2 (V x H). The X-ray beam incident angle was set at 0.5°, and the Rayonix lx255-HS area detector with a pixel size of 88.54 x 88.54 um2 was employed to record the scattering pattern. The reciprocal space was calibrated using Cr_2O_3 as standard, obtaining the detector tilts and a sample to detector distance of 101.44 mm. Grazing incidence total X-ray scattering measurements[71] of the samples were performed at the ID15A beamline of the European Synchrotron Radiation Facility (ESRF), France.[72] The beam energy was 64 keV and the beam was focused to a size of 2.5-3 μm (V) by 6 μm (H) using refractive lenses in the beam path 3 m before the sample. Data were acquired with a Pilatus3 X CdTe 2M detector for an incidence angle of the order of 0.025-0.035° and a sample-to-detector distance of 222.29 mm, calibrated using NIST standard Cr_2O_3 powder. Measurements of a blank Si sample were also acquired for background subtraction. The intense diffraction spots originating from Si were masked in the 2D diffraction patterns, followed by azimuthal

integration. The background subtracted 1D patterns were transformed into pair distribution functions (PDF) using PDFgetX3,[73] applying a Q_{max} value of 22.0 Å^{-1}. PDF refinements were carried out in TOPAS Academic version 7.[74]The fit residual is defined as $R_p = \left[\sum_i \left(Y_{O,i} - Y_{C,i}\right)^2 / \sum_i \left(Y_{O,i}\right)^2\right]^{1/2}$, with $Y_{O,i}$ and $Y_{C,i}$ the experimental (observed) and calculated data in point *i*.

For gas-phase analysis of the reaction products, *in situ* quadrupole mass spectrometry (QMS, Hiden Analytical) was performed. Gas species were ionized with an energy of 70 eV and detected with a secondary electron multiplier detector. Before the QMS characterization was done, the chamber and sample stage were precoated by several hundreds of RuO_2 ALD cycles. Temperatures were the same as for the regular depositions. For the characterization of the RuO_4 pulse, 100 iterations of the following cycle were carried out: (Open valve to mass spectrometer) + (20 s wait time) + 3*(40 s RuO_4 + 40 s pump time) + (close valve to mass spectrometer) + (20 s wait time) + (25 s methanol + 20 s pump time). For the characterization of the methanol pulse, the following variation was used, as well 100 times: (open valve to mass spectrometer) + (20 s wait time) + 3*(25 s methanol + 20 s pump time) + (close valve to mass spectrometer) + (20 s wait time) + (40 s RuO_4 + 40 s pump time). After data analysis according to a method described earlier in more detail[75] a time-resolved spectrum of the full range of masses was obtained (see **Figure S9**). Relevant slices of this spectrum, resembling conventional, time-resolved measurements at specific m/z are presented in the main manuscript, as they are more straightforward to interpret.

In vacuo XPS experiments were performed in order to obtain the oxidation state of Ru in the deposited films. The experiments were performed on a dedicated ALD-XPS setup consisting of a Theta Probe XPS instrument (Thermo Fisher Scientific Inc.) directly connected to a custom-built ALD reactor.[76-77] This allows sample transfer between ALD reactor (10^{-7} mbar) and XPS (10^{-10} mbar) in less than a minute and without (high) vacuum break. The XPS spectra were calibrated with respect to the Si-$2p_{3/2}$ peak at 99.4 eV.

A Vertex 70v vacuum spectrometer from Bruker was used to measure the mid-IR spectra of the thin films in transmission mode during the ALD process on double polished Si wafer. Each mid-IR spectrum is the average of 200 scans, resulting in a measurement time of ca. 200 s. Spectra were collected at the start of every

experiment, after each ALD reaction and at the end of the process. The FTIR spectra were analyzed using the OPUS software package from Bruker.

Results and Discussion

In this section, we first present the ALD characteristics and thin film properties for the process using RuO_4 and methanol as the reactants. Next, we show that the RuO_2 growth rate can be tuned by selecting a different type of alcohol, more specifically for ethanol, 1-propanol and 2-propanol. Finally, we propose a reaction mechanism for the process, based on the learnings acquired by *in situ* QMS, *in situ* FTIR and *in vacuo* XPS studies.

Growth characteristics of the RuO_2 ALD process

The self-limiting behavior of the two reactions is an important aspect of an ALD process. Saturation experiments for the RuO_4-methanol process were performed on Si-H substrates at a substrate temperature of 100 °C. **Figure 1a** and **1b** show the saturation curves for RuO_4 and methanol, respectively. First, the pulse time of RuO_4 was varied while keeping the methanol pulse time fixed at 25s. Saturation of the surface reaction with RuO_4 was achieved at 40s, with a GPC of 1Å/cycle. Similar experiments were conducted to reveal the saturation behavior of the surface reaction with the methanol precursor at a fixed pulsing time of 40s for the RuO_4 precursor. These experiments indicated saturation for the methanol reaction at about 20s. Next, the dependence of ALD growth on the temperature was evaluated using the saturated conditions for both reactions. Only temperatures below 125 °C were studied, as the RuO_4 precursor is known to thermally decompose above this substrate temperature.[59] The GPC remained the same throughout the temperature range studied (60 °C - 120 °C), slightly above 1Å/cycle (**Figure 1c)**.

The linearity of the process was studied by *ex situ* XRR (**Figure 1d**). Depositions with different cycle numbers were performed on both Si-H and Si with native oxide substrates at a deposition temperature of 100 °C. The pulse time for methanol was 25s and for RuO_4 the pulse time was 40s. These experiments revealed that the thickness of the films increased linearly with the number of ALD cycles with an average GPC of 1Å per cycle on both substrates, and without a significant nucleation delay. Comparing the nucleation behavior of the RuO_4-methanol process with the RuO_4-H_2

process,[76] it can be concluded that both processes behave similar on H-terminated Si, demonstrating swift nucleation. In contrast, for ALD on Si with a native oxide, the RuO_4-H_2 process was marked by initial inhibited growth, while this is not observed in **Figure 1d** for the RuO_4-methanol process. As RuO_4 is a strong oxidizer, the immediate growth on Si-H was explained by RuO_4 oxidizing the Si during the first exposure, while the lack of a surface that can be further oxidized explains the inhibited growth on SiO_2. We reported that one single pre-pulse of TMA on an oxide surface allows the growth of Ru metal without growth inhibition, as RuO_4 will oxidize the CH_3 groups of the adsorbed TMA molecules.[76] The linear growth on Si with native oxide observed in **Figure 1d** suggests that methanol molecules reside on the surface following the first exposure, which can act as similar nucleation sites for RuO_4 as the aforementioned TMA molecules.

The conformality of an ALD process is very important, as it is the ability to deposit films on high aspect ratio (AR) structures, with preferably no variation in the amount and the composition of the material deposited along the structures.[51, 78] The conformality of the RuO_2 coating was evaluated by depositing 100 cycles on silicon micropillars with an equivalent AR (EAR) of approximately 10 (namely, 2 μm wide and 50 μm high pillars, spaced at a 4 μm center-to-center distance on a square lattice) etched into a silicon substrate as shown in **Figure 1e.**[78] After the deposition, the sample was analyzed in cross section with scanning electron microscopy (SEM) and energy-dispersive X-ray spectroscopy (EDX) to evaluate the amount of ruthenium at different depths along the pillar. The EDX spectrum (**Figure 1f**) indicated clear ruthenium signals at all depths. Although there is a slight variation in the Ru signal at different depths, the signal intensity at 50 μm depth is still comparable with the Ru signal intensity at the top of the pillar which suggests a decent conformality of the process (note that variations can be due to the slightly conical shape of the pillars).

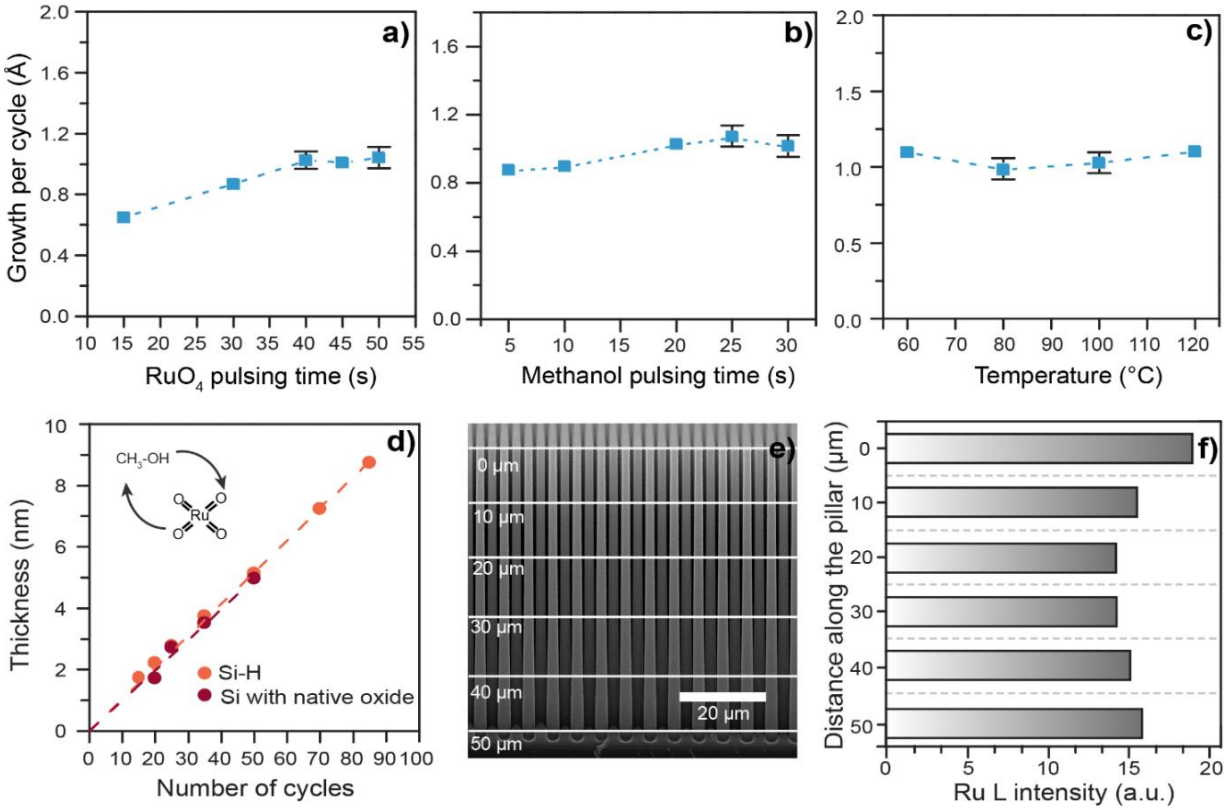

Figure 1: ALD characteristics: **a)** Growth per cycle (GPC) as a function of RuO_4 pulse time, using a fixed pulse time of 25s for methanol. **b)** GPC as a function of methanol pulse time, with the RuO_4 pulse time kept fixed at 40s. **c)** Temperature window of the ALD process showing the growth per cycle as a function of substrate temperature, as obtained from XRR. Note that for the data points with error bars, the mean of the data points measured in each case is plotted and the error bar corresponds to the standard deviation of the data. **d)** Thickness vs. the number of ALD cycles, as determined from XRR on Si-H and Si with native oxide substrates at 100 °C (Inset: schematic illustration of the ALD process). **e)** Cross-sectional SEM image of the RuO_2 coated micropillars indicating the different depths where the EDX was measured. **f)** The normalised Ru L

Material Characterization

To verify that the films deposited using the RuO_4-methanol process are ruthenium dioxide, *in vacuo* XPS measurements were carried out. For reference purposes, first, a metallic Ru film was deposited using the previously reported RuO_4-H_2 ALD process.[59] In a second experiment, a film was deposited using the RuO_4-methanol

ALD process under study. In both cases, 15 cycles were performed on a Si-H substrate and the samples were transferred to the XPS analysis chamber immediately after deposition and without high vacuum break. The XPS spectra were calibrated by placing the Si-$2p_{3/2}$ peak of the substrate at 99.4 eV.[79] The XPS signal from the substrate is visible as the films have a thickness of about 2 nm, which is below the information depth for XPS.[80] Inspection of the Ru 3d XPS spectra clearly indicates differences in binding energy and shape between the two films (**Figure 2a)**. For metallic Ru, the Ru $3d_{5/2}$ and Ru $3d_{3/2}$ peaks are observed at 280.4 eV and 284.6 eV, respectively, and the peaks have a FWHM of 0.6 eV and 0.9 eV, consistent with Ru(0) (see **Figure S1**).[81] For the film deposited with the RuO_4-methanol process, the Ru $3d_{5/2}$ and Ru $3d_{3/2}$ peaks are positioned at 281.1 eV and 285.3 eV, respectively, and they are much broader compared to metallic Ru. The 0.7 eV shift of the Ru $3d_{5/2}$ peak towards higher binding energy compared to Ru(0), is consistent with a +4 oxidation state of the Ru atoms.[82-84] The broad nature of the Ru 3d peaks is also expected for pure RuO_2, and originates from satellite peaks induced by XPS final-state effects.[85] Morgan *et al.*[81] performed a detailed XPS study on Ru-containing materials, and the models they reported for metallic ruthenium and ruthenium dioxide were used to deconvolute and fit the Ru 3d and O 1s peaks (**Figure 2b** and **2c**, respectively). The O 1s spectrum contains two different components, attributed to Ru-O and Ru-O-H bonds[81, 86-87] (**Figure 2c**). The results of the fits are tabulated in Supporting Information, and the good agreement with the earlier reported models allows us to conclude that the films deposited with the RuO_4-methanol process are RuO_2.[81] Concerning the impurity content of the RuO_2 films, we note that determining the carbon content in the films with XPS is a challenge due to the overlap of the C 1s with the Ru 3d region and the complex satellite structure of the Ru 3d spectrum. The peak fitting results, where the constraints used in the model are based on the reference work by Morgan *et al*.[81], yielded a carbon concentration below 5%, providing an indication that the carbon contamination in the as-deposited RuO_2 thin films is acceptably low. Fluorine impurities (2 at. %) were also detected with *in vacuo* XPS, most likely deriving from the methyl-ethyl fluorinated solvent used in the ToRuS precursor.[66] The fluorine could be removed by short Ar^+ ion etching, which suggests that the fluorine is not built into the films and is only present at the surface. No other impurities than carbon and fluorine were detected.

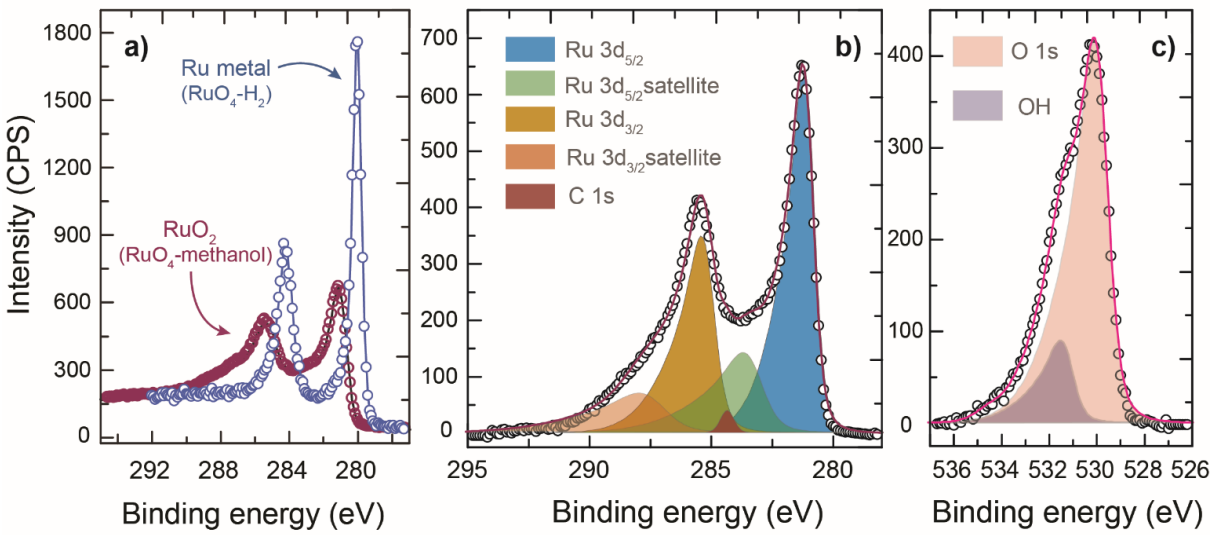

Figure 2: a) Comparison of the *in vacuo* XPS spectra in the Ru 3d region for metallic Ru (RuO_4-H_2 ALD process)[58], and RuO_2 (RuO_4-methanol process, this work). **b)** and **c)** XPS peak deconvolution of the Ru 3d and O 1s signals, respectively for the RuO_4-methanol process.

The crystallinity of the RuO_2 films was investigated by various X-ray scattering methods. Conventional lab-based XRD measurements did not reveal any diffraction signal for as-deposited films of 20 nm thickness (**Figure 3a**), suggesting that the as-deposited RuO_2 thin film would be amorphous. As several of the applications require crystalline RuO_2, we investigated the crystallization of the RuO_2 films by post-deposition thermal annealing. For this, 20 nm RuO_2 films deposited on Si-H were annealed up to a temperature of 800 °C in helium, and in air, both with a ramp rate of 0.2°C/s. During each anneal, the RuO_2 crystallization was monitored by lab-based *in situ* XRD (**Figure 3b, c**). At around 420°C, clear diffraction peaks originating from crystalline rutile RuO_2 start to appear during both anneals. After cooling down to room temperature, *ex situ* XRD measurements were performed, and the data are displayed in **Figure 3a** (blue and yellow pattern), showing that the diffraction peaks can be identified based on the rutile RuO_2 diffractogram (JCPDS 88-0322). To learn more about the carbon content in the RuO_2 thin films before and after crystallization, SIMS measurements were carried out and the results are presented in **Figure S2**. SIMS revealed a lower level of carbon impurities in the film after the anneal.

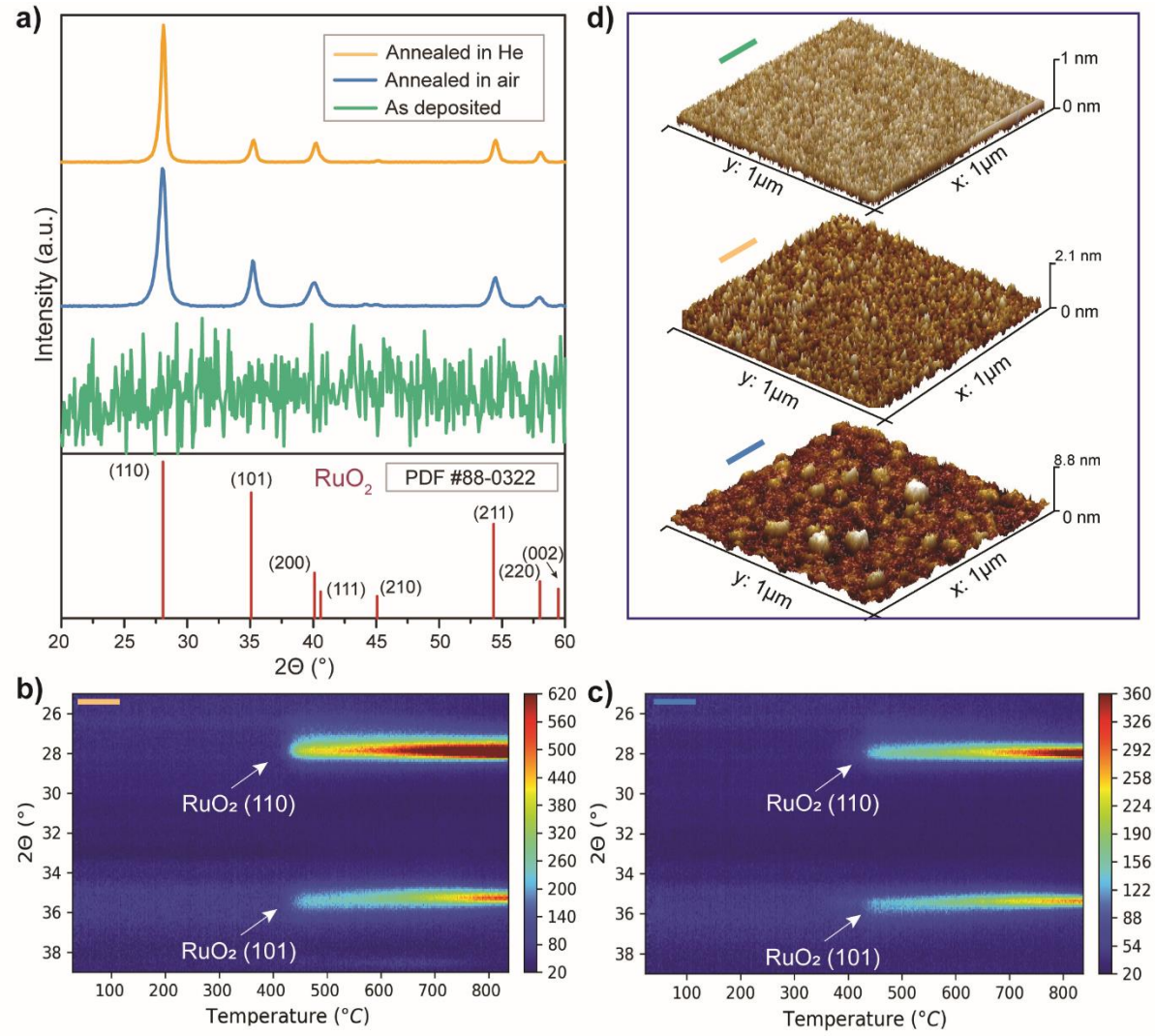

Figure 3: a) Lab-based *ex situ* X-ray diffractograms of as-deposited, He-annealed, and air-annealed RuO_2 films with a thickness of 20 nm. **b) and c)** *In situ* XRD patterns acquired during the anneals in helium and air, respectively. **d)** 3D AFM images of an as-deposited 20 nm RuO_2 film on a Si-H substrate (top), the same film after annealing in He to 800 °C (middle), and after annealing in air to 800 °C (bottom). Note the different scales along the z-axis (height).

The film morphology of the as-deposited and the post-annealed RuO_2 films was studied by atomic force microscopy (AFM). The as-deposited film (20 nm thick, prepared using the RuO_4-methanol process) was found to be relatively smooth with an RMS roughness value of 0.48 nm (**Figure 3d,** top). The roughness value increases to 0.88 nm after the anneal in He (**Figure 3d,** middle). The air annealed films show an even higher roughness value of 2.85 nm (**Figure 3d,** bottom). The increase in roughness after the anneal can be attributed to grain formation during

crystallization. The higher roughness for the air-annealed films could potentially be related to the diffusion of oxygen atoms (in the air ambient) into the film during the anneal. [88-89]

Finally, the crystallization of as-deposited RuO_2 was compared with the formation of crystalline RuO_2 by the oxidation of metallic Ru films (grown with the RuO_4-H_2 ALD process) as depicted in **Figure S3a**. The crystallization of as-deposited RuO_2 occurred around 400-450°C, whereas the oxidation of metallic Ru to crystalline RuO_2 requires temperatures as high as 600 °C. Moreover, the former process resulted in smoother films and the latter in rough RuO_2 layers, as evident from the SEM images in **Figure S3b**. The rough RuO_2 layer formation is likely related to the volume change associated to oxidation.

To further investigate the structural properties of the as-deposited and annealed RuO_2 thin films, grazing incidence wide angle X-ray scattering (GIWAXS) measurements as well as grazing incidence total X-ray scattering measurements with pair distribution function analysis (GIPDF) were carried out for 50 nm thick films before and after anneal in helium. **Figure 4a** and **b** show the 2D GIWAXS patterns for the as-deposited and annealed layer that were recorded at the NCD-SWEET beamline of the ALBA synchrotron, Spain. Intense diffraction rings can be observed for the annealed sample, as expected, while also for the as-deposited layer diffraction rings are visible, be it more broad and less intense signals. In **Figure 4c**, the azimuthal integrated patterns are shown. In line with the lab-based XRD measurements, the diffraction peaks of the annealed thin film can be identified based on the rutile RuO_2 phase. In contrast, the broad diffractions for the as-deposited material match the diffractogram of Ru hcp metal. Together with the XPS results confirming the growth of RuO_2, this suggests a microstructure of amorphous RuO_2 with nanocrystalline Ru inclusions that could not be detected with lab-based XRD.

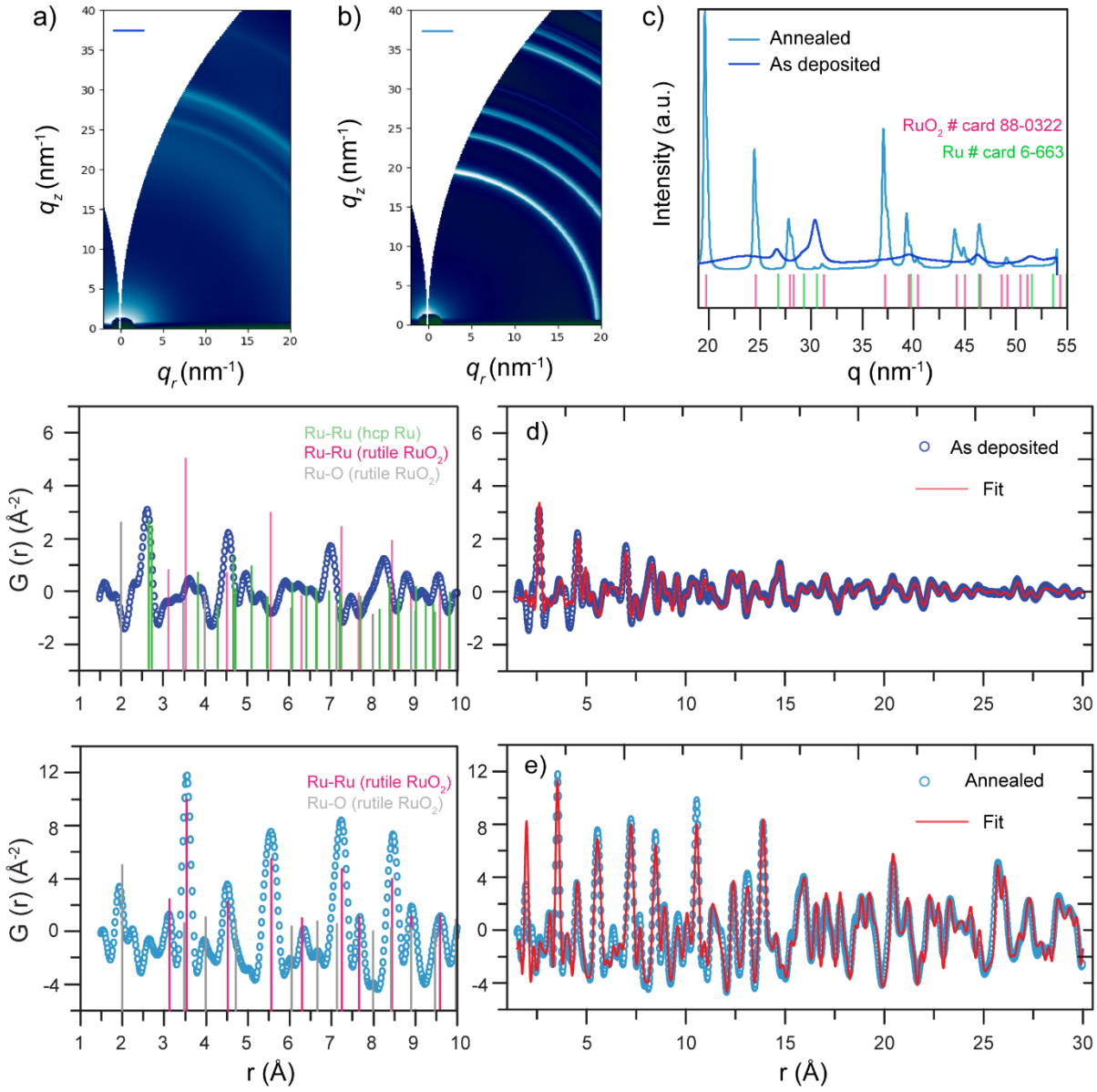

Figure 4: a) and b) Synchrotron-based 2D GIWAXS patterns of a 50 nm as-deposited film and of the same film annealed in helium. **c)** Azimuthal integration of the GIWAXS data for the two films**. d) and e)** PDFs of the as-deposited and the annealed films, resulting from the grazing incidence total X-ray scattering patterns shown in **Figure S4**. The respective zoomed images are provided in the left side of the plots.

Total scattering experiments employing a grazing incidence geometry have recently been proposed to access the local and medium range order of atoms in thin films, whether crystalline or not, via PDF analysis. Here, we applied the emerging GIPDF method[71, 73] to further clarify the structure of the as-deposited RuO_2 thin films by comparing its PDF to the one of the crystalline annealed material. **Figure 4d** and **4e** show the extracted PDF for the as-deposited and annealed sample, respectively. The

zooms on the left side include the bond distances for ideal bulk rutile RuO_2 and Ru hcp metal.[90-91] The PDF for the annealed sample exhibits significant oscillations to at least 50 Å, indicative of long-range order, as expected for a crystalline thin film (**Figure S5**). The Ru-Ru bond lengths dominate the PDF of the rutile RuO_2 structure due to the larger scattering power of Ru compared to O. It can be seen that the positions of the dominant peaks in the experimental PDF agree with the expected Ru-Ru bond lengths in an ideal rutile RuO_2 structure.[91] Fitting the data against models of rutile RuO_2 and Ru hcp in the range between 1.5 and 30 Å confirms that the thin film structure resembles that of the rutile RuO_2 structure. A good agreement with the experimental PDF is obtained for a model assuming 99 wt% of RuO_2 (R_p = 0.24). The peaks in the PDF for the as-deposited sample decay to zero faster, yet the presence of clear features up to 22 Å indicates that the film exhibits local structural order. The observed pair correlations, however, differ in position and amplitude when compared with the structure that is adopted after thermal annealing. In this case, the experimental PDF, especially the features at larger *r*-values, can be fitted best against a model that is dominated by the hexagonal Ru structure (96 wt%, R_p = 0.30), in line with the reciprocal space data revealing diffractions corresponding to hcp Ru. Comparison of the pattern with the ideal model of rutile RuO_2 in the range up to 4 Å also reveals some resemblance. A peak can be observed at ~1.95 Å, which corresponds to the first Ru-O bond distance in rutile RuO_2. The second Ru-Ru peak, expected to be the most intense Ru-Ru correlation, at ~ 3.54 Å, is also visible. and a weak feature, corresponding to the first Ru-Ru bond distance, can be discerned at ~3.1 Å. For these *r*-values, no overlap with Ru-Ru correlations in hcp Ru is expected. Overall this hints towards amorphous RuO_2 that exhibits only short range order at the level of the nearest neighbors, while the structural order seen for larger distances is mostly a consequence of the nanocrystalline Ru hcp inclusions. Nevertheless, this investigation highlights that ALD-grown thin films that are easily classified as “amorphous” based on lab-based XRD measurements, can actually present structural medium to long range order that may often remain under the radar.

The electrical resistivity of the films was determined using four-point probe measurements. The resistivity of an as-deposited 20 nm RuO_2 film (on Si with native oxide substrate) was found to be 230 μΩ.cm. The resistivity values improved upon thermal annealing to 800 °C in both air and He. After the anneal in air, the resistivity

value decreased to 199 μΩ·cm and after the anneal in He, the resistivity was 123 μΩ·cm. These values indicate a fairly conductive RuO_2 film, and they are comparable with existing literature reports for ALD-synthesized RuO_2.[41] The resistivity improvement after the anneals may be associated with the introduction of crystallinity in the samples and decrease in carbon content.

The optical properties were assessed by performing *ex situ* transmittance measurements using spectroscopic ellipsometry for the RuO_2 (ca. 15 nm) film deposited on a quartz substrate. The results and analysis details are explained in Supporting Information (**Figure S6**). A value of 1.9 eV was obtained as the band gap for the RuO_2 films, comparable with other reports.[92-93]

Growth using other alcohols as the co-reactant

The ALD characteristics and film properties of the RuO_4-methanol process have been explained in detail. It is known that RuO_4 can react with both primary and secondary alcohols in solution, and different by-products are obtained depending on the choice of the alcohol.[94] Therefore, we performed a series of depositions combining RuO_4 with ethanol, 1-propanol, and 2-propanol (isopropanol) as the co-reactants. The depositions were performed on H-terminated Si substrates at a temperature of 100°C. As shown in **Figure 5a**, growth occurred for each of the alcohols at the conditions studied. Interestingly, the growth rate increases with the carbon chain length. While the growth rate for the methanol-based process is 1 Å/cycle, the growth rates for the ethanol and 1-propanol based processes increase to 1.4 Å/cycle and 2 Å/cycle, respectively. The 2-propanol-based process displays the same growth rate as the 1-propanol-based process.

The saturation behavior of these processes was investigated. Just like the experiments with methanol, H-terminated silicon was chosen as the substrate, and it was kept at 100 °C. From **Figure 5b and 5c,** it follows that the saturation conditions are independent of the choice of the alcohol. Saturation was achieved after 40s for the RuO_4 pulses and 25s for the alcohol pulses in all cases. To reveal if the choice of the alcohol influences the roughness of the films, *ex situ* AFM measurements were performed on samples of similar thickness **(Figure 5d**). It was found that the RMS roughness of the as-deposited RuO_2 increases with increase in the length of the

carbon chain. More specifically, for methanol, a 20 nm film had a roughness of 0.48 nm. For the ethanol, 2-propanol, and 1-propanol based processes, the RMS values were 0.81 nm (9.7 nm film), 1.2 nm (10 nm film), and 0.92 nm (11 nm film), respectively.

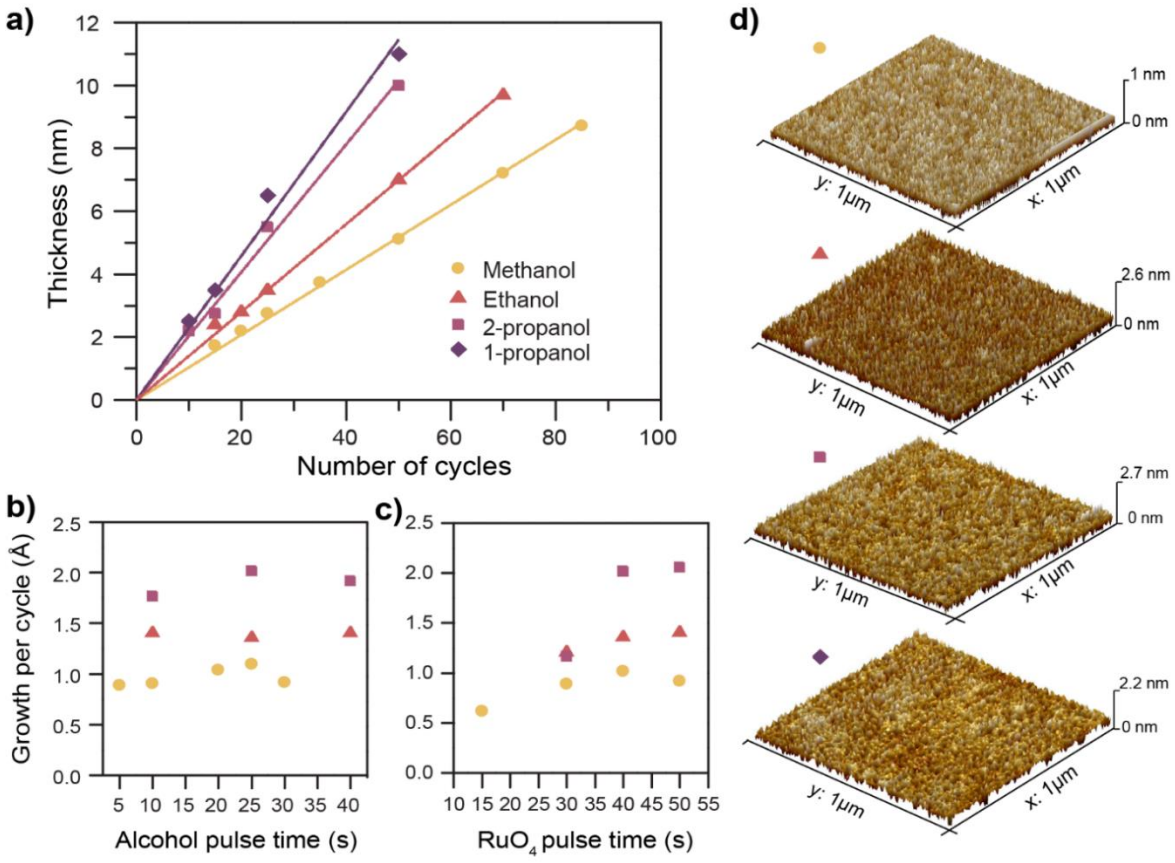

Figure 5: a) Thickness against the number of ALD cycles for the methanol, ethanol, 1-propanol, and 2-propanol (isopropanol) based processes, as obtained from XRR. **b)** and **c)** Saturation curves for the RuO_4 surface reaction and the alcohol surface reaction, respectively, for these different processes. **d)** 3D-AFM images obtained for the methanol, ethanol, 2-propanol, and 1-propanol based processes (from top to bottom respectively) after 85, 70, 50, and 50 ALD cycles, respectively. Note the different scales along the z-axis (height).

Lab-based *ex situ* XRD before and after annealing, and *in situ* XRD measurements during annealing, did not reveal significant differences in the crystallization behavior of films deposited with different alcohols. No diffraction peaks could be observed for the as-deposited films, which crystallize into rutile RuO_2 by annealing in either inert atmosphere or in air. The *ex situ* XRD patterns recorded after annealing reveal

differences in preferential crystallographic orientation with different annealing atmosphere (**Figure S7**), which was not observed for the RuO_2 material deposited with methanol (**Figure 3a**). The onset of crystallization was around 420°C in all cases (**Figure S8**). This latter result provides an indirect indication that the carbon content in the films grown with different alcohols is comparable as a larger carbon contamination is known to often result in an increase in crystallization temperature.[95] The resistivity values for the films deposited using methanol (12 nm RuO_2), ethanol (9.7 nm), 2-propanol (10 nm) were 245 μΩ·cm, 282 μΩ·cm, 322 μΩ·cm respectively, which are also comparable**.**

Mechanism of the developed ALD process

In situ QMS, *in situ* FTIR and *in vacuo* XPS were used to gain insights into the mechanism of the developed process by probing the gas phase reaction products and surface chemistry. In QMS, data can only be obtained for a single mass at a time, and the common approach in ALD research is to follow a couple of selected masses to confirm or disprove a certain hypothesis on the reaction mechanism. Recently, our group showed that it is possible to exploit the cyclic nature of ALD to obtain full mass-over-charge spectra, in a time-resolved fashion, to screen for the formation of any reaction products during the two reactions in the ALD cycle.[66] Time-resolved full-range mass spectra were collected during the methanol and RuO_4 surface reactions with the methodology described in our earlier work (**Figure S9**). Relevant parts from those full-range spectra are shown in **Figure 6a** for the methanol reaction and in **Figure 6b** for the RuO_4 reaction, respectively. During the collection of mass spectra, molecules entering the spectrometer will be ionized and fragmented. It is relevant to note that different fragments of the same parent molecule may have a different absolute intensity, but the time evolution of this intensity will be very similar as it is directly correlated to the partial pressure of the parent molecule.

Methanol (m/z 32) will be fragmented in the mass spectrometer (**Figure 6a**), hence the CH_3 fragment with m/z 15 presents a reference for the partial pressure of methanol. The water signal (m/z 18) is transient, which identifies it as a reaction product. The fragment at m/z 44 can be attributed to CO_2. It is not transient, but because it is heavier than methanol, it must be a reaction product as well. No other signals above m/z 32 were observed during the methanol pulse. The appearance of H_2O and CO_2 in the spectrum can therefore be attributed to the oxidation of methanol by the RuO_2 surface.

This observation is backed up by other reports, showing that under vacuum conditions, CH_3OH is oxidized to CO_2 on a RuO_2 surface.[96] As a result, the RuO_2 surface will be partially reduced.

During the RuO_4 pulse, a myriad of fragments is present in the time-resolved, full-range spectrum. Most of those fragments do not originate from the RuO_4 molecule itself, but from the proprietary solvent complex that is used for the safe handling of the precursor. When analyzing all fragments, three distinct types of time evolutions were discerned (**Figure 6b**). A first type of time evolution that we observed was linked to the partial pressure of unreacted precursor in the chamber. As the signal for the Ru atom itself (m/z 101) had a very low intensity, the fragment with m/z 32 (possibly O_2) is shown in Figure 6b. Most fragments that are related to the solvent showed this type of time evolution. A second type of time evolution was observed for mass 44. As can be seen in Figure 6b, this signal shows a transient behavior, and the first peak is longer-lasting (broader in time) and more intense than that of the RuO_4/solvent type. This kind of time evolution was only observed for m/z 44 and can be attributed to the formation of CO_2 as a reaction product during the RuO_4 pulse. Hence, there must be carbon left at the surface after the methanol pulse. Finally, a third, distinct shape of time evolution was found for some fragments of the solvent complex. As an example, the fragment with m/z 81 is presented in **Figure 6b**. As can be seen in the time evolution of this fragment, a peak arises with a time delay relative to the peak of the CO_2 signal, and it also displays a transient behavior. We can explain this as follows: the RuO_4 molecules enter the chamber in a complex with the solvent molecules. Upon reaction of this RuO_4-solvent complex with the surface, CO_2 is formed as a reaction product, and RuO_x is incorporated into the film. After this reaction, the solvent molecules leave the surface, leading to a time delay in the QMS data.

To investigate if carbon species are accumulating on the surface during the methanol pulse and are removed during the RuO_4 pulse (as seen by CO_2 evolution in the mass spectrometry), *in situ* FTIR experiments were performed (**Figure 6c**). The changes that occur at the surface during the methanol pulse (referenced to the previous RuO_4 pulse) and RuO_4 pulse (referenced to the previous methanol pulse) are shown in difference spectra in **Figure 6c.** The positive features represent the chemical groups that are being added and negative features the groups that are being removed during each pulse. During the methanol pulse, the significant peak that appeared (positive feature, marked by a dotted line) was around 2000cm^{-1}, which is attributed to CO

adsorbed on the RuO_2 surface during the methanol oxidation on RuO_2. This peak has been previously linked to CO adsorption on coordinatively unsaturated Ru on RuO_2 surfaces.[97] The complete removal of this peak was observed during the RuO_4 pulse as seen by the negative feature in the same region, indicating that CO is oxidized to CO_2, corroborating the mass spectrometry data. There are, however, some weak features to be seen after the methanol pulse around 1147 cm^{-1} and 1049 cm^{-1}, which are most likely related to the methoxy species (CH_3-O)[98] originating from the oxidation of methanol on the RuO_2 surface.

To further support the QMS data, *in vacuo* XPS measurements were carried out. The RuO_4-methanol process was conducted on a Si-H substrate for 100 cycles, and the sample was transferred to the XPS without (high) vacuum break after the RuO_4 pulse followed by the acquisition of the O 1s spectrum (**Figure 6d**). After this, the same sample was transferred back to the ALD chamber to perform two additional ALD cycles, this time for the process ending with methanol, after which again the O 1s spectrum was acquired. In both cases (for the process ending with RuO_4 and for the one ending with methanol) the spectra can be deconvoluted into two different components, one at a binding energy of 529.7 eV and the other at 530.1 eV. The one at 529.7 eV can be attributed to a Ru-O bond[81, 86] and the one at 531.1 eV to Ru-O-H[81, 87, 99] bonds. Note that the contribution of the Si substrate (oxidized during the growth) in the O 1s signal is excluded by the absence of a Si 2p peak measured after 100 cycles of the methanol-RuO_4 process (see **Figure S10**). Inspection of the O 1s spectra in the figure clearly indicates a lower oxygen signal for the process ending with methanol compared to the one ending with RuO_4. This in turn suggests that during the methanol pulse the top surface of the RuO_2 film is reduced to RuO_x ($0 \leq x < 2$). The OH component was not found to be affected by the RuO_4 or methanol treatment. Han et al. reported the CVD of RuO_2 using RuO_4 and H_2 gas where they proposed that hydroxyl groups can be formed due to the interaction of H_2 with RuO_2. Such groups can also favor the chemisorption of RuO_4. In contrary, we did not find a substantial decrease in OH intensity after the RuO_4 pulse, indicating less (no) reaction of RuO_4 with hydroxyl groups on the surface. However, a similar mechanism as in our case was observed when methanol decomposition was studied on a RuO_2 surface, where, RuO_2 catalyzes the oxidation of methanol to different products, depending on the conditions chosen and as a result of this the RuO_2 top layer is reduced to metallic Ru or RuO_x.[100] Similar to the O 1s regions, the Ru 3d regions (for the processes ending

with RuO_4 and for the one ending with methanol) were also examined, as shown in **Figure S11**. However, no useful inference can be drawn in this case due to the complex satellite structure of the Ru 3d region.

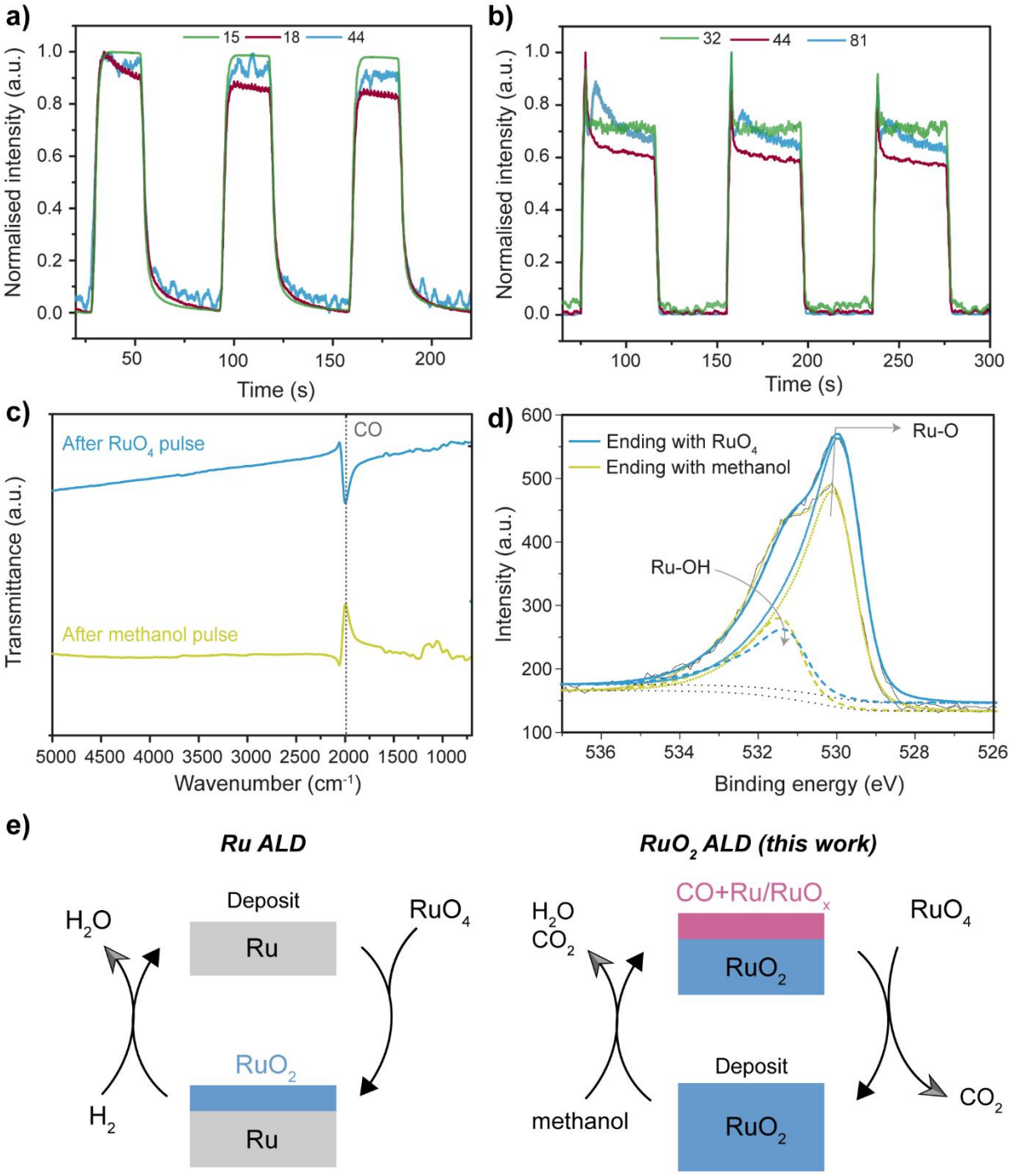

Figure 6: a) , b) *In situ* mass spectrometry data obtained during successive methanol pulses and successive RuO_4 pulses, respectively **c)** *In situ* FTIR difference spectra for the methanol (blue) and RuO_4 half cycles (red). The methanol difference spectrum is

acquired by subtracting the FTIR spectrum acquired after the RuO_4 pulse from that acquired after the subsequent methanol pulse, and vice versa. **d)** *In vacuo* XPS spectra acquired in the O 1s region. The blue and yellow spectra indicate processes ending with RuO_4 and methanol, respectively. The dotted lines indicate the Ru-O components, and the dashed lines indicate the Ru-OH components. **e)** The proposed reaction mechanisms for Ru ALD and RuO_2 ALD (this work).

These experiments helped us to put forward a plausible mechanism for the developed process. A schematic illustration is provided in **Figure 6e**, which includes also the inferred mechanism of the Ru ALD[59] process for comparison. For Ru ALD with RuO_4 and H_2, in the first half cycle, the Ru surface is oxidized by the RuO_4 molecules, bounding RuO_2 to the surface in a self-saturating way. In the second reaction, H_2 gas enables the reduction of RuO_2 to metallic Ru. For RuO_2 ALD with RuO_4 and methanol, our results indicate that the alcohol (during the alcohol pulse) is oxidized into CO_2 and H_2O on a RuO_2 surface. As a result of this oxidation, CO remains present at the surface. The oxidation of methanol in turn leads to the reduction of the surface RuO_2 to a slightly O_2 deficient RuO_2 surface. The detection of nanocrystalline Ru inclusion in the as-deposited material provides another hint that the alcohol indeed leads to a reduction of the RuO_2 surface. RuO_4 can easily nucleate on such a reduced RuO_x/Ru surface layer which helps to oxidize (during the next RuO_4 pulse) the surface again to a thicker and oxygen-rich RuO_2. The CO that was present on the surface is oxidized and leaves the surface as CO_2.

Conclusion

We have demonstrated a novel ALD synthesis strategy for depositing RuO_2 thin films utilizing the reaction between RuO_4 and alcohols. The reaction of methanol with RuO_4 yielded a GPC of 1Å/cycle exhibiting all typical characteristics of an ALD process, without a significant nucleation delay. Interestingly, the GPC could be tuned by altering the alcohol counterpart. The GPC was found to be 1.4 Å/cycle when using ethanol, and it was around 2 Å/cycle when using 1-propanol and 2-propanol. Irrespective of the chosen alcohol, amorphous RuO_2 thin films were deposited. Structural characterization with synchrotron-based grazing incidence X-ray scattering methods revealed the presence of nanocrystalline Ru metal inclusions in the as-deposited

amorphous RuO_2 films. However, post-deposition annealing either in He or in air yielded crystalline rutile RuO_2 around 420°C. Highly conductive films were obtained as evident from the resistivity value of 230 μΩ cm for the as-deposited films of 20 nm thickness and this value is found to improve after annealing. The as-deposited films were found to be smooth with RMS roughness of 0.48 nm. Annealing in He resulted in only slight increase in the roughness (0.88 nm), whereas after annealing in air, the RMS roughness increased to a value of 2.8 nm. The mechanism of the developed ALD process was investigated with *in situ* mass spectrometry, *in situ* FTIR and *in vacuo* XPS. This indicated oxidation of methanol on the RuO_2 surface yielding CO_2 and H_2O as by-products and concomitant reduction of the RuO_2 top layer to metallic Ru or RuO_x. The methanol pulse also leaves some CO residues on the surface. The reduced RuO_2 surface is then oxidized back to a thicker RuO_2 surface again during the next RuO_4 pulse with the removal of CO on the surface as CO_2.

ASSOCIATED CONTENT

Supporting Information

Ru 3d XPS spectra of Ru metal, XPS fitting parameters and details. SIMS data before and after anneal, ex-situ and in-situ XRD for processes using different alcohols, total X-ray scattering data and PDF data for the annealed film, band gap calculation of RuO_2 films, in situ mass spectrometry data heat maps, *in vacuo* XPS spectra acquired in the Ru 3d region.

AUTHOR INFORMATION

Corresponding Author

*Email: Jolien.Dendooven@UGent.be

Conflicts of interest

There are no conflicts of interest to declare.

Author Contributions

∇ N.P. and M.M.M. contributed equally to this work.

Acknowledgements

This project has received funding from the European Union's Horizon 2020 research and innovation program under the Marie Skłodowska-Curie grant agreement no. 765378. The authors would like to acknowledge Air Liquide for supplying the ToRuS precursor. We thank Ranjith. K. Ramachandran for useful discussions. Matthias Minjauw and Andreas Werbrouck would like to thank the Flemish Research Foundation (FWO-Vlaanderen). The Special Research Fund BOF of Ghent University (GOA 01G01513) is also acknowledged. Dr. Alexander Merkulov is thanked for performing the SIMS measurements.

The ESRF is acknowledged for provision of beamtime under proposal number MA-4987(doi.esrf.fr/10.15151/ESRF-ES-538779994). The GIWAXS experiments were performed at the NCD-SWEET beamline at ALBA Synchrotron with the collaboration of ALBA staff.

References

1. Han, J. H.; Han, S.; Lee, W.; Lee, S. W.; Kim, S. K.; Gatineau, J.; Dussarrat, C.; Hwang, C. S., Improvement in the Leakage Current Characteristic of Metal-Insulator-Metal Capacitor by Adopting Ruo2 Film as Bottom Electrode. *Applied Physics Letters* **2011**, *99*, 022901.
2. Majumdar, D.; Maiyalagan, T.; Jiang, Z., Recent Progress in Ruthenium Oxide-Based Composites for Supercapacitor Applications. *ChemElectroChem* **2019**, *6*, 4343-4372.
3. Ryden, W.; Lawson, A.; Sartain, C. C., Electrical Transport Properties of Ir O 2 and Ru O 2. *Physical Review B* **1970**, *1*, 1494.
4. Trasatti, S., Physical Electrochemistry of Ceramic Oxides. *Electrochimica Acta* **1991**, *36*, 225-241.
5. Zheng, J.; Cygan, P.; Jow, T., Hydrous Ruthenium Oxide as an Electrode Material for Electrochemical Capacitors. *Journal of the Electrochemical Society* **1995**, *142*, 2699.
6. Hu, C.-C.; Chen, W.-C.; Chang, K.-H., How to Achieve Maximum Utilization of Hydrous Ruthenium Oxide for Supercapacitors. *Journal of the Electrochemical Society* **2004**, *151*, A281.
7. Zheng, J.; Jow, T., A New Charge Storage Mechanism for Electrochemical Capacitors. *Journal of the Electrochemical Society* **1995**, *142*, L6.
8. Bharali, P.; Kuratani, K.; Takeuchi, T.; Kiyobayashi, T.; Kuriyama, N., Capacitive Behavior of Amorphous and Crystalline Ruo2 Composite Electrode Fabricated by Spark Plasma Sintering Technique. *Journal of Power Sources* **2011**, *196*, 7878-7881.
9. Wen, T. C.; Hu, C. C., Hydrogen and Oxygen Evolutions on Ru-Ir Binary Oxides. *Journal of the Electrochemical Society* **1992**, *139*, 2158.
10. Chalupczok, S.; Kurzweil, P.; Hartmann, H.; Schell, C., The Redox Chemistry of Ruthenium Dioxide: A Cyclic Voltammetry Study—Review and Revision. *International Journal of Electrochemistry* **2018**, *2018*.
11. Han, J.; An, H. J.; Kim, T.-W.; Lee, K.-Y.; Kim, H. J.; Kim, Y.; Chae, H.-J., Effect of Structure-Controlled Ruthenium Oxide by Nanocasting in Electrocatalytic Oxygen and Chlorine Evolution Reactions in Acidic Conditions. *Catalysts* **2019**, *9*, 549.

12. Kuratani, K.; Tanaka, H.; Takeuchi, T.; Takeichi, N.; Kiyobayashi, T.; Kuriyama, N., Binderless Fabrication of Amorphous Ruo2 Electrode for Electrochemical Capacitor Using Spark Plasma Sintering Technique. *Journal of Power Sources* **2009**, *191*, 684-687.
13. Zhang, J.-R.; Chen, B.; Li, W.-K.; Zhu, J.-J.; Jiang, L.-P., Electrochemical Behavior of Amorphous Hydrous Ruthenium Oxide/Active Carbon Composite Electrodes for Super-Capacitor. *International Journal of Modern Physics B* **2002**, *16*, 4479-4483.
14. Nguyen, N., *Synthesis of Ruthenium (Iv) Oxide (Ruo 2) Nanocrystals*; University of South Dakota, 2012.
15. Over, H., Surface Chemistry of Ruthenium Dioxide in Heterogeneous Catalysis and Electrocatalysis: From Fundamental to Applied Research. *Chemical Reviews* **2012**, *112*, 3356-3426.
16. Trasatti, S., Electrocatalysis: Understanding the Success of Dsa®. *Electrochimica Acta* **2000**, *45*, 2377-2385.
17. Cui, X.; Zhou, J.; Ye, Z.; Chen, H.; Li, L.; Ruan, M.; Shi, J., Selective Catalytic Oxidation of Ammonia to Nitrogen over Mesoporous Cuo/Ruo2 Synthesized by Co-Nanocasting-Replication Method. *Journal of Catalysis* **2010**, *270*, 310-317.
18. Seki, K., Development of Ruo 2/Rutile-Tio 2 Catalyst for Industrial Hcl Oxidation Process. *Catalysis surveys from Asia* **2010**, *14*, 168-175.
19. Liu, H.; Iglesia, E., Selective Oxidation of Methanol and Ethanol on Supported Ruthenium Oxide Clusters at Low Temperatures. *The Journal of Physical Chemistry B* **2005**, *109*, 2155-2163.
20. Majumdar, D., An Overview on Ruthenium Oxide Composites–Challenging Material for Energy Storage Applications. *Material Science Research India* **2018**, *15*, 30-40.
21. Xia, H.; Meng, Y. S.; Yuan, G.; Cui, C.; Lu, L., A Symmetric Ruo2/Ruo2 Supercapacitor Operating at 1.6 V by Using a Neutral Aqueous Electrolyte. *Electrochemical and Solid State Letters* **2012**, *15*, A60.
22. Hu, C. C.; Huang, Y. H., Cyclic Voltammetric Deposition of Hydrous Ruthenium Oxide for Electrochemical Capacitors. *Journal of the Electrochemical Society* **1999**, *146*, 2465.
23. Ahn, Y. R.; Song, M. Y.; Jo, S. M.; Park, C. R.; Kim, D. Y., Electrochemical Capacitors Based on Electrodeposited Ruthenium Oxide on Nanofibre Substrates. *Nanotechnology* **2006**, *17*, 2865.
24. Hassan, A. S.; Navulla, A.; Meda, L.; Ramachandran, B. R.; Wick, C. D., Molecular Mechanisms for the Lithiation of Ruthenium Oxide Nanoplates as Lithium-Ion Battery Anode Materials: An Experimentally Motivated Computational Study. *The Journal of Physical Chemistry C* **2015**, *119*, 9705-9713.
25. Kim, Y.; Muhammad, S.; Kim, H.; Cho, Y. H.; Kim, H.; Kim, J. M.; Yoon, W. S., Probing the Additional Capacity and Reaction Mechanism of the Ruo2 Anode in Lithium Rechargeable Batteries. *ChemSusChem* **2015**, *8*, 2378-2384.
26. Krusin-Elbaum, L.; Wittmer, M.; Yee, D., Characterization of Reactively Sputtered Ruthenium Dioxide for Very Large Scale Integrated Metallization. *Applied physics letters* **1987**, *50*, 1879-1881.
27. Meng, L.-j.; Teixeira, V.; Dos Santos, M., Raman Spectroscopy Analysis of Magnetron Sputtered Ruo2 Thin Films. *Thin Solid Films* **2003**, *442*, 93-97.
28. Meng, L.-J.; Dos Santos, M., A Study of Residual Stress on Rf Reactively Sputtered Ruo2 Thin Films. *Thin Solid Films* **2000**, *375*, 29-32.
29. Lim, J. H.; Choi, D. J.; Cho, W. I.; Yoon, Y. S., Ruo 2 Sputtered Thin Film Supercapacitor's Performance as Function of Oxygen Incorporation. *Journal of the Korean Physical Society* **2001**, *39*.
30. Fang, X.; Tachiki, M.; Kobayashi, T. In *Deposition and Properties of Pld Grown Ruo2 Thin Film*, Third International Conference on Thin Film Physics and Applications, International Society for Optics and Photonics: 1998; pp 331-335.
31. Hiratani, M.; Matsui, Y.; Imagawa, K.; Kimura, S., Growth of Ruo2 Thin Films by Pulsed-Laser Deposition. *Thin Solid Films* **2000**, *366*, 102-106.
32. Zhitomirsky, I.; Gal-Or, L., Ruthenium Oxide Deposits Prepared by Cathodic Electrosynthesis. *Materials Letters* **1997**, *31*, 155-159.

33. Hu, C.-C.; Chang, K.-H., Cyclic Voltammetric Deposition of Hydrous Ruthenium Oxide for Electrochemical Capacitors: Effects of Codepositing Iridium Oxide. *Electrochimica Acta* **2000**, *45*, 2685-2696.
34. Lakshminarayana, G.; Kityk, I.; Nagao, T., Synthesis, Structural, and Electrical Characterization of Ruo 2 Sol–Gel Spin-Coating Nano-Films. *Journal of Materials Science: Materials in Electronics* **2016**, *27*, 10791-10797.
35. Cheng, C.; Chen, Y.; Chen, R.; Huang, Y., Raman Scattering and Field-Emission Properties of Ruo 2 Nanorods. *Applied Physics Letters* **2005**, *86*, 103104.
36. Si, J.; Desu, S. B., Ruo 2 Films by Metal-Organic Chemical Vapor Deposition. *Journal of materials research* **1993**, *8*, 2644-2648.
37. Swider-Lyons, K. E.; Love, C. T.; Rolison, D. R., Selective Vapor Deposition of Hydrous Ruo2 Thin Films. *Journal of the Electrochemical Society* **2005**, *152*, C158.
38. Yuan, Z.; Puddephatt, R. J.; Sayer, M., Low-Temperature Chemical Vapor Deposition of Ruthenium Dioxide from Ruthenium Tetroxide: A Simple Approach to High-Purity Ruo2 Films. *Chemistry of materials* **1993**, *5*, 908-910.
39. Wang, X.; Gordon, R. G., High-Quality Epitaxy of Ruthenium Dioxide, Ruo2, on Rutile Titanium Dioxide, Tio2, by Pulsed Chemical Vapor Deposition. *Crystal growth & design* **2013**, *13*, 1316-1321.
40. Jung, H. J.; Han, J. H.; Jung, E. A.; Park, B. K.; Hwang, J.-H.; Son, S. U.; Kim, C. G.; Chung, T.-M.; An, K.-S., Atomic Layer Deposition of Ruthenium and Ruthenium Oxide Thin Films from a Zero-Valent (1, 5-Hexadiene)(1-Isopropyl-4-Methylbenzene) Ruthenium Complex and O2. *Chemistry of Materials* **2014**, *26*, 7083-7090.
41. Austin, D. Z.; Jenkins, M. A.; Allman, D.; Hose, S.; Price, D.; Dezelah, C. L.; Conley Jr, J. F., Atomic Layer Deposition of Ruthenium and Ruthenium Oxide Using a Zero-Oxidation State Precursor. *Chemistry of Materials* **2017**, *29*, 1107-1115.
42. Methaapanon, R.; Geyer, S. M.; Bent, S. F., The Low Temperature Atomic Layer Deposition of Ruthenium and the Effect of Oxygen Exposure. *Journal of Materials Chemistry* **2012**, *22*, 25154-25160.
43. Kim, W. H.; Park, S. J.; Kim, H., Atomic Layer Deposition of Ruthenium and Ruthenium-Oxide Thin Films by Using a Ru (Etcp) 2 Precursor and Oxygen Gas. *Journal of the Korean Physical Society* **2009**, *55*, 32-37.
44. Yeo, S.; Park, J.-Y.; Lee, S.-J.; Lee, D.-J.; Seo, J. H.; Kim, S.-H., Ruthenium and Ruthenium Dioxide Thin Films Deposited by Atomic Layer Deposition Using a Novel Zero-Valent Metalorganic Precursor,(Ethylbenzene)(1, 3-Butadiene) Ru (0), and Molecular Oxygen. *Microelectronic Engineering* **2015**, *137*, 16-22.
45. Schaefer, M.; Schlaf, R., Electronic Structure Investigation of Atomic Layer Deposition Ruthenium (Oxide) Thin Films Using Photoemission Spectroscopy. *Journal of Applied Physics* **2015**, *118*, 065306.
46. Kwon, O.-K.; Kim, J.-H.; Park, H.-S.; Kang, S.-W., Atomic Layer Deposition of Ruthenium Thin Films for Copper Glue Layer. *Journal of the Electrochemical Society* **2004**, *151*, G109.
47. Kwon, S.-H.; Kwon, O.-K.; Kim, J.-H.; Jeong, S.-J.; Kim, S.-W.; Kang, S.-W., Improvement of the Morphological Stability by Stacking Ruo2 on Ru Thin Films with Atomic Layer Deposition. *Journal of the Electrochemical Society* **2007**, *154*, H773.
48. Park, S.-J.; Kim, W.-H.; Maeng, W.; Yang, Y.; Park, C.; Kim, H.; Lee, K.-N.; Jung, S.-W.; Seong, W., Effect Oxygen Exposure on the Quality of Atomic Layer Deposition of Ruthenium from Bis (Cyclopentadienyl) Ruthenium and Oxygen. *Thin Solid Films* **2008**, *516*, 7345-7349.
49. Park, J.-Y.; Yeo, S.; Cheon, T.; Kim, S.-H.; Kim, M.-K.; Kim, H.; Hong, T. E.; Lee, D.-J., Growth of Highly Conformal Ruthenium-Oxide Thin Films with Enhanced Nucleation by Atomic Layer Deposition. *Journal of alloys and compounds* **2014**, *610*, 529-539.
50. Kim, J.-H.; Kil, D.-S.; Yeom, S.-J.; Roh, J.-S.; Kwak, N.-J.; Kim, J.-W., Modified Atomic Layer Deposition of Ru O 2 Thin Films for Capacitor Electrodes. *Applied Physics Letters* **2007**, *91*, 052908.
51. Detavernier, C.; Dendooven, J.; Sree, S. P.; Ludwig, K. F.; Martens, J. A., Tailoring Nanoporous Materials by Atomic Layer Deposition. *Chemical Society Reviews* **2011**, *40*, 5242-5253.

52. George, S. M., Atomic Layer Deposition: An Overview. *Chemical reviews* **2010**, *110*, 111-131.
53. Leskelä, M.; Ritala, M., Atomic Layer Deposition (Ald): From Precursors to Thin Film Structures. *Thin solid films* **2002**, *409*, 138-146.
54. Salaün, A.; Newcomb, S. B.; Povey, I. M.; Salaün, M.; Keeney, L.; O'mahony, A.; Pemble, M. E., Nucleation and Chemical Transformation of Ruo2 Films Grown on (100) Si Substrates by Atomic Layer Deposition. *Chemical Vapor Deposition* **2011**, *17*, 114-122.
55. Kim, J.-H.; Ahn, J.-H.; Kang, S.-W.; Roh, J.-S.; Kwon, S.-H.; Kim, J.-Y., Thermal Stability of Ruo2 Thin Films Prepared by Modified Atomic Layer Deposition. *Current Applied Physics* **2012**, *12*, S160-S163.
56. Hušeková, K.; Dobročka, E.; Rosová, A.; Šoltýs, J.; Šatka, A.; Fillot, F.; Fröhlich, K., Growth of Ruo2 Thin Films by Liquid Injection Atomic Layer Deposition. *Thin Solid Films* **2010**, *518*, 4701-4704.
57. Aaltonen, T.; Rahtu, A.; Ritala, M.; Leskelä, M., Reaction Mechanism Studies on Atomic Layer Deposition of Ruthenium and Platinum. *Electrochemical and Solid State Letters* **2003**, *6*, C130.
58. Kim, S. K.; Hoffmann-Eifert, S.; Waser, R., Growth of Noble Metal Ru Thin Films by Liquid Injection Atomic Layer Deposition. *The Journal of Physical Chemistry C* **2009**, *113*, 11329-11335.
59. Minjauw, M. M.; Dendooven, J.; Capon, B.; Schaekers, M.; Detavernier, C., Atomic Layer Deposition of Ruthenium at 100° C Using the Ruo 4-Precursor and H 2. *Journal of Materials Chemistry C* **2015**, *3*, 132-137.
60. Minjauw, M. M.; Dendooven, J.; Capon, B.; Schaekers, M.; Detavernier, C., Near Room Temperature Plasma Enhanced Atomic Layer Deposition of Ruthenium Using the Ruo 4-Precursor and H 2-Plasma. *Journal of Materials Chemistry C* **2015**, *3*, 4848-4851.
61. Satta, A.; Shamiryan, D.; Baklanov, M. R.; Whelan, C. M.; Le, Q. T.; Beyer, G. P.; Vantomme, A.; Maex, K., The Removal of Copper Oxides by Ethyl Alcohol Monitored in Situ by Spectroscopic Ellipsometry. *Journal of The Electrochemical Society* **2003**, *150*, G300.
62. Chalker, P.; Romani, S.; Marshall, P.; Rosseinsky, M.; Rushworth, S.; Williams, P., Liquid Injection Atomic Layer Deposition of Silver Nanoparticles. *Nanotechnology* **2010**, *21*, 405602.
63. Sarr, M.; Bahlawane, N.; Arl, D.; Dossot, M.; McRae, E.; Lenoble, D., Tailoring the Properties of Atomic Layer Deposited Nickel and Nickel Carbide Thin Films Via Chain-Length Control of the Alcohol Reducing Agents. *The Journal of Physical Chemistry C* **2014**, *118*, 23385-23392.
64. Huo, J.; Solanki, R.; McAndrew, J., Characteristics of Copper Films Produced Via Atomic Layer Deposition. *Journal of materials research* **2002**, *17*, 2394-2398.
65. Musschoot, J.; Xie, Q.; Deduytsche, D.; Van den Berghe, S.; Van Meirhaeghe, R.; Detavernier, C., Atomic Layer Deposition of Titanium Nitride from Tdmat Precursor. *Microelectronic Engineering* **2009**, *86*, 72-77.
66. Gatineau, J.; Yanagita, K.; Dussarrat, C., A New Ruo4 Solvent Solution for Pure Ruthenium Film Depositions. *Microelectronic Engineering* **2006**, *83*, 2248-2252.
67. Knaepen, W.; Detavernier, C.; Van Meirhaeghe, R.; Sweet, J. J.; Lavoie, C., In-Situ X-Ray Diffraction Study of Metal Induced Crystallization of Amorphous Silicon. *Thin Solid Films* **2008**, *516*, 4946-4952.
68. Knaepen, W.; Gaudet, S.; Detavernier, C.; Van Meirhaeghe, R.; Sweet, J. J.; Lavoie, C., In Situ X-Ray Diffraction Study of Metal Induced Crystallization of Amorphous Germanium. *Journal of Applied Physics* **2009**, *105*, 083532.
69. Ramachandran, R. K.; Dendooven, J.; Botterman, J.; Sree, S. P.; Poelman, D.; Martens, J. A.; Poelman, H.; Detavernier, C., Plasma Enhanced Atomic Layer Deposition of Ga2o3 Thin Films. *Journal of Materials Chemistry A* **2014**, *2*, 19232-19238.
70. Majeed, B.; Zhang, L.; Tutunjyan, N.; Jones, B.; Fiorini, P.; Tezcan, D. S. In *Silicon Micro-Pillar Filter Fabrication for DNA Separation in Lab-on-Chip System*, 2012 IEEE 14th Electronics Packaging Technology Conference (EPTC), IEEE: 2012; pp 52-56.
71. Dippel, A.-C.; Roelsgaard, M.; Boettger, U.; Schneller, T.; Gutowski, O.; Ruett, U., Local Atomic Structure of Thin and Ultrathin Films Via Rapid High-Energy X-Ray Total Scattering at Grazing Incidence. *IUCrJ* **2019**, *6*, 290-298.

72. Vaughan, G. B.; Baker, R.; Barret, R.; Bonnefoy, J.; Buslaps, T.; Checchia, S.; Duran, D.; Fihman, F.; Got, P.; Kieffer, J., Id15a at the Esrf–a Beamline for High Speed Operando X-Ray Diffraction, Diffraction Tomography and Total Scattering. *Journal of synchrotron radiation* **2020**, *27*, 515-528.
73. Juhás, P.; Davis, T.; Farrow, C. L.; Billinge, S. J., Pdfgetx3: A Rapid and Highly Automatable Program for Processing Powder Diffraction Data into Total Scattering Pair Distribution Functions. *Journal of Applied Crystallography* **2013**, *46*, 560-566.
74. TOPAS, C. A., Topas-Academic: An Optimization Program Integrating Computer Algebra and Crystallographic Objects Written in C++ J. *Appl. Crystallogr* **2018**, *51*, 210-218.
75. Werbrouck, A.; Shirazi, M.; Mattelaer, F.; Elliott, S. D.; Dendooven, J.; Detavernier, C., A Secondary Reaction Pathway for the Alumina Atomic Layer Deposition Process with Trimethylaluminum and Water, Revealed by Full-Range, Time-Resolved in Situ Mass Spectrometry. *The Journal of Physical Chemistry C* **2020**, *124*, 26443-26454.
76. Minjauw, M. M.; Rijckaert, H.; Driessche, I. V.; Detavernier, C.; Dendooven, J., Nucleation Enhancement and Area-Selective Atomic Layer Deposition of Ruthenium Using Ruo4 and H2 Gas. *Chemistry of Materials* **2019**, *31*, 1491-1499.
77. Vandenbroucke, S. S.; Levrau, E.; Minjauw, M. M.; Van Daele, M.; Solano, E.; Vos, R.; Dendooven, J.; Detavernier, C., Study of the Surface Species During Thermal and Plasma-Enhanced Atomic Layer Deposition of Titanium Oxide Films Using in Situ Ir-Spectroscopy and in Vacuo X-Ray Photoelectron Spectroscopy. *Physical Chemistry Chemical Physics* **2020**, *22*, 9262-9271.
78. Cremers, V.; Puurunen, R. L.; Dendooven, J., Conformality in Atomic Layer Deposition: Current Status Overview of Analysis and Modelling. *Applied Physics Reviews* **2019**, *6*, 021302.
79. Thøgersen, A.; Selj, J. H.; Marstein, E. S., Oxidation Effects on Graded Porous Silicon Anti-Reflection Coatings. *Journal of the Electrochemical Society* **2012**, *159*, D276.
80. Powell, C. J., Practical Guide for Inelastic Mean Free Paths, Effective Attenuation Lengths, Mean Escape Depths, and Information Depths in X-Ray Photoelectron Spectroscopy. *Journal of Vacuum Science & Technology A: Vacuum, Surfaces, and Films* **2020**, *38*, 023209.
81. Morgan, D. J., Resolving Ruthenium: Xps Studies of Common Ruthenium Materials. *Surface and Interface Analysis* **2015**, *47*, 1072-1079.
82. Rochefort, D.; Dabo, P.; Guay, D.; Sherwood, P., Xps Investigations of Thermally Prepared Ruo2 Electrodes in Reductive Conditions. *Electrochimica Acta* **2003**, *48*, 4245-4252.
83. Basinska, A.; Stoch, J.; Domka, F., Xps Study of Ru-Fe2o3 Catalysts for the Water-Gas Shift Reaction. *Polish Journal of Environmental Studies* **2003**, *4*.
84. Chan, H. Y. H.; Takoudis, C. G.; Weaver, M. J., High-Pressure Oxidation of Ruthenium as Probed by Surface-Enhanced Raman and X-Ray Photoelectron Spectroscopies. *journal of catalysis* **1997**, *172*, 336-345.
85. Cox, P.; Goodenough, J.; Tavener, P.; Telles, D.; Egdell, R., The Electronic Structure of Bi2−Xgdxru2o7 and Ruo2: A Study by Electron Spectroscopy. *Journal of Solid State Chemistry* **1986**, *62*, 360-370.
86. Mun, C.; Ehrhardt, J.; Lambert, J.; Madic, C., Xps Investigations of Ruthenium Deposited onto Representative Inner Surfaces of Nuclear Reactor Containment Buildings. *Applied Surface Science* **2007**, *253*, 7613-7621.
87. Asim, S.; Javed, M. S.; Hussain, S.; Rana, M.; Iram, F.; Lv, D.; Hashim, M.; Saleem, M.; Khalid, M.; Jawaria, R., Ruo2 Nanorods Decorated Cnts Grown Carbon Cloth as a Free Standing Electrode for Supercapacitor and Lithium Ion Batteries. *Electrochimica Acta* **2019**, *326*, 135009.
88. Wang, R.; Beling, C.; Fung, S.; Djurišić, A.; Ling, C.; Li, S., Influence of Gaseous Annealing Environment on the Properties of Indium-Tin-Oxide Thin Films. *Journal of applied physics* **2005**, *97*, 033504.
89. Chang, J.; Lin, W.; Hon, M.-H., Effects of Post-Annealing on the Structure and Properties of Al-Doped Zinc Oxide Films. *Applied Surface Science* **2001**, *183*, 18-25.

90. Kumara, L.; Sakata, O.; Kohara, S.; Yang, A.; Song, C.; Kusada, K.; Kobayashi, H.; Kitagawa, H., Origin of the Catalytic Activity of Face-Centered-Cubic Ruthenium Nanoparticles Determined from an Atomic-Scale Structure. *Physical Chemistry Chemical Physics* **2016**, *18*, 30622-30629.
91. Dmowski, W.; Egami, T.; Swider-Lyons, K. E.; Love, C. T.; Rolison, D. R., Local Atomic Structure and Conduction Mechanism of Nanocrystalline Hydrous Ruo2 from X-Ray Scattering. *The Journal of Physical Chemistry B* **2002**, *106*, 12677-12683.
92. Patake, V.; Lokhande, C., Chemical Synthesis of Nano-Porous Ruthenium Oxide (Ruo2) Thin Films for Supercapacitor Application. *Applied Surface Science* **2008**, *254*, 2820-2824.
93. El-Tantawy, F.; Al-Ghamdi, A. A.; Al-Ghamdi, A. A.; Al-Turki, Y. A.; Alshahrie, A.; Al-Hazmi, F.; Al-Hartomy, O. A., Optical Properties of Nanostructured Ruthenium Dioxide Thin Films Via Sol–Gel Approach. *Journal of Materials Science: Materials in Electronics* **2017**, *28*, 52-59.
94. Lee, D. G.; van den Engh, M., The Oxidation of Organic Compounds by Ruthenium Tetroxide. In *Organic Chemistry*, Elsevier: 1973; Vol. 5, pp 177-227.
95. Song, X.; Takoudis, C. G., Cyclic Chemical-Vapor-Deposited Tio2⁄ Al2o3 Film Using Trimethyl Aluminum, Tetrakis (Diethylamino) Titanium, and O2. *Journal of The Electrochemical Society* **2007**, *154*, G177.
96. Latimer, A. A.; Abild-Pedersen, F.; Nørskov, J. K., A Theoretical Study of Methanol Oxidation on Ruo2 (110): Bridging the Pressure Gap. *ACS Catalysis* **2017**, *7*, 4527-4534.
97. Adeyemo, A.; Hunter, G.; Dutta, P. K., Interaction of Co with Hydrous Ruthenium Oxide and Development of a Chemoresistive Ambient Co Sensor. *Sensors and Actuators B: Chemical* **2011**, *152*, 307-315.
98. Boccuzzi, F.; Chiorino, A.; Manzoli, M., Ftir Study of Methanol Decomposition on Gold Catalyst for Fuel Cells. *Journal of power sources* **2003**, *118*, 304-310.
99. Barison, S.; Barreca, D.; Daolio, S.; Fabrizio, M.; Tondello, E., Influence of Electrochemical Processing on the Composition and Microstructure of Chemical-Vapor Deposited Ru and Ruo 2 Nanocrystalline Films. *Journal of Materials Chemistry* **2002**, *12*, 1511-1518.
100. Blume, R.; Hävecker, M.; Zafeiratos, S.; Teschner, D.; Knop-Gericke, A.; Schlögl, R.; Dudin, P.; Barinov, A.; Kiskinova, M., Oxidation of Methanol on Ru Catalyst: Effect of the Reagents Partial Pressures on the Catalyst Oxidation State and Selectivity. *Catalysis today* **2007**, *124*, 71-79.

TOC Graphic